Effect of Model Tear Film Lipid Layer on Water Evaporation

Xiaojie Xu,[1] Guangle Li,[1] and Yi Y. Zuo[1,2]

[1]Department of Mechanical Engineering, University of Hawaii at Manoa, Honolulu, Hawaii, United States
[2]Department of Pediatrics, John A. Burns School of Medicine, University of Hawaii, Honolulu, Hawaii, United States

Correspondence: Yi Y. Zuo, 2540 Dole St, Holmes Hall 302, Honolulu, HI 96822, USA; yzuo@hawaii.edu.

PURPOSE. A majority of in vitro models were incapable of reproducing the evaporation resistance of tear film lipid layer (TFLL) in vivo. The purpose of this research is to develop a novel in vitro model to study the effect of TFLL on water evaporation.

METHODS. A ventilated, closed-chamber, droplet evaporimeter with a constant surface area has been invented to study the evaporation resistance of TFLL. This evaporimeter ensures a rigorous control of environmental conditions, including the temperature, relative humidity, airflow rate, surface area, and surface pressure, thus allowing for reproducible water evaporation measurements over a time period of only 5 minutes. The volumetric evaporation rate of this droplet evaporimeter is less than 2.7 µL/min, comparable to the basal tear production of healthy adults. Together with direct film imaging using atomic force microscopy (AFM), we have studied the effect of a model TFLL on water evaporation, as a function of the lipid composition and surface pressure.

RESULTS. A model TFLL composed of 40% wax esters, 40% cholesteryl esters, and 20% polar lipids was capable of reducing the water evaporation rate by 11% at surface pressure 47 mN/m. AFM revealed that the model TFLL at high surface pressures consists of discrete droplets/aggregates of the nonpolar lipids residing atop a polar lipid monolayer with phase separation.

CONCLUSIONS. The TFLL may resist water evaporation with a combined mechanism by increasing film compactness of the polar lipid film at the air-water surface, and, to a lesser extent, by increasing film thickness of the nonpolar lipid film.

Keywords: atomic force microscopy (AFM), constrained drop surfactometry, droplet, dry eye disease, evaporimeter, surface tension, tear film lipid layer (TFLL), water evaporation

Tear film is a multilayered biological barrier covering the ocular surface to protect and lubricate the cornea.[1] The tear film can be divided into three distinct layers: an inner mucus layer with sugar-rich glycosylated proteins, an aqueous layer with dissolved proteins, metabolites, and electrolytes, and an outmost lipid layer made up of various lipid species.[2,3] This lipid layer, commonly known as the tear film lipid layer (TFLL), is approximately 100 nm thick.[4] The current consensus is that the TFLL consists of two sublayers: a polar lipid layer at the air-water surface, mainly consisting of phospholipids and (O-acyl)-ω-hydroxy fatty acids (OAHFAs), and a nonpolar lipid layer, composed of wax esters and cholesteryl esters, residing atop the polar lipid layer and directly exposing to the environment.[5–7] Nonpolar lipids in the TFLL are secreted by the meibomian glands, whereas the source of phospholipids in the TFLL is still uncertain.[8] The polar lipids may facilitate spreading of the nonpolar lipids, rather than forming aggregations or droplets, over the aqueous surface of the tear film.[9,10]

The TFLL has multiple physiological functions, such as host defense against ocular infection and retardation of water evaporation.[11–15] Water evaporation is one of the most important mechanisms for tear film thinning.[16] Rapid water evaporation leads to increased tear film instability and premature breakup, which happens in evaporative dry eye.[13,17] In general, dysfunction of the TFLL results in dry eye disease that affects 10% to 30% of the world population.[18–20]

Although it is generally accepted that the TFLL helps reduce water evaporation in vivo,[21–25] in vitro findings remain controversial. Most in vitro studies with meibomian lipid films and model tear film lipids only demonstrated relatively insignificant or nearly no retardation to water evaporation.[26–32] These controversial results were likely related to the in vitro models used for studying water evaporation. Quantitative study of monolayer retardation on water evaporation can be traced back to the seminal work by Victor La Mer in the 1950s for the interests of conserving water in reservoirs.[33–35] To date, a vast majority of these in vitro studies relied on the classical Langmuir trough,[26–32] which has a few limitations that prevent accurate evaluation of water evaporation. First, due to its large size, the Langmuir trough generally lacks a rigorous control in environmental conditions, such as the temperature, relative humidity, and airflow rate, all of which are essential factors that can significantly affect the rate of water evaporation. Second, the evaporation rate is traditionally determined with gravimetric analysis (i.e. directly measuring the mass of water lost

by evaporation from a Langmuir trough), which requires a relatively long period of experiments (usually 0.5–2 hours) to reduce system errors.[27] This further increases the difficulty of environmental control during such an extended period of experiments. Third, Langmuir trough can hardly reproduce the physiologically relevant high surface pressure of the TFLL. The surface tension of whole tears of healthy individuals was reported to be around 43 to 46 mN/m,[36,37] which most likely represents the surface tension of major proteins in tears, such as lysozyme.[38] Upon film compression during the blinking process, the TFLL can reduce the surface tension to approximately 20 mN/m, corresponding to a surface pressure as high as 50 mN/m.[38,39] However, most existing in vitro evaporation studies only covered the surface pressure range between 5 and 30 mN/m, because the TFLL rapidly collapses at higher surface pressures in a Langmuir trough. Hence, there is an urgent need for alternative biophysical models to evaluate the effect of TFLL on water evaporation under physiologically relevant conditions.

Here, we developed a novel droplet-based biophysical model to study the effect of TFLL on water evaporation. Owing to system miniaturization, droplet-based evaporation models offer a more rigorous environmental control than the classical Langmuir trough. Both pendant drop[40] and sessile drop[41] methods have been attempted in previous studies. A key novelty of this work was the invention of a ventilated, closed-chamber, droplet evaporimeter with a constant surface area, analogous to the evaporimeter used for measuring the tear evaporation rate in vivo.[24,42,43] This in vitro evaporimeter was realized with the combination of constrained drop surfactometry and a novel feedback control system called closed loop-axisymmetric drop shape analysis that decoupled surface area of the droplet from water evaporation. Using this novel biophysical model, together with direct film imaging using atomic force microscopy, we have studied the effect of a model TFLL on water evaporation. Our data suggest that the model TFLL is capable of reducing the water evaporation rate by 11% at high surface pressures. Our experimental results may provide novel implications into better understanding the biophysical and physiological function of the TFLL.

METHODS

Materials

Dipalmitoyl phosphatidylcholine (DPPC), L-α-phosphatidylcholine (PC) from egg yolk, palmitic-acid-9-hydroxy-stearic-acid (PAHSA), and cholesteryl oleate (CO) were purchased from Sigma-Aldrich (St. Louis, MO, USA). Behenyl oleate (BO) was purchased from Larodan (Monroe, MI, USA). Physicochemical properties of these lipids can be found elsewhere.[38] Individual lipids were dissolved in chloroform as 1 mM stock solutions. Water used was Milli-Q ultrapure water with a resistivity greater than 18 M$\Omega\cdot$cm at room temperature.

Constrained Drop Surfactometry

Constrained drop surfactometry (CDS) is a new generation of droplet-based surface tensiometry technique developed in our laboratory.[44,45] It uses the air-water surface of a millimeter-sized sessile drop to accommodate the spread or adsorbed film. As shown in Figure 1, a key design

of the CDS is a carefully machined pedestal that uses its knife-sharp edge to prevent film leakage even at very low surface tensions. System miniaturization of the CDS facilitates rigorous control of experimental conditions with an environmental control chamber. The spread/adsorbed film at the droplet surface can be compressed and expanded by precisely controlling oscillation of the surface area of the droplet using a newly developed mechatronic system called closed-loop axisymmetric drop shape analysis (CL-ADSA).[46] The CL-ADSA determines the surface tension of the spread/adsorbed film by analyzing the shape of the film-covered droplet. The surface pressure (π) can be determined from the surface tension (γ) using $\pi = \gamma_0$-γ, with γ_0 being the surface tension of a clean, lipid-free air-water surface.

Specifically, a trace amount of the lipid sample was spread onto the air-water surface of a 15 µL droplet serving as the aqueous subphase to the spread lipid film. The spread film was left undisturbed for 1 minute to allow evaporation of the solvent and to reach equilibrium. The droplet was then slowly expanded to decrease the surface pressure to around zero (i.e. increasing the surface tension to around 70 mN/m). Subsequently, the spread lipid film was compressed quasi-statically at a rate of 0.15 A%/s to a target surface pressure.

Ventilated Closed-Chamber Droplet Evaporimeter With a Constant Surface Area

Figure 1 illustrates the schematic of the droplet-based evaporimeter. Lipid samples were spread onto the air-water surface of a 5-mm droplet (27 µL in volume and 0.35 cm^2 in surface area) to result in a target surface pressure. The environmental temperature and relative humidity (RH) were controlled at 34.0 $\pm$ 0.1°C and 33.0 $\pm$ 2.0% with a closed environmental control chamber. The chamber was ventilated with a continuous airflow. The airflow rate was measured with a hot wire anemometer (TSI, Shoreview, MN, USA) and was controlled at 1.0 $\pm$ 0.1 m/s to simulate the ambient environment.[47]

A key feature of the droplet-based evaporimeter is its capacity of maintaining a constant surface area during water evaporation. As shown in Figure 1, CL-ADSA maintains the constant surface area of a droplet by determining its surface area in real-time and feeding this information back to a motorized syringe to automatically complete a proportional-integral-derivative (PID) control loop.[46] The evaporation rate (mm/min) was calculated as ($\Delta V/\Delta t)/A_{drop}$, where ΔV was the volume of water replenished into the droplet, in order to compensate for the evaporated water and thus to maintain the constant surface area. The Δt is the time period of the experiment (i.e. 5 minutes). The $\Delta V/\Delta t$ was determined from linear regression of the recorded ΔV-Δt curve. The A_{drop} was the surface area of the droplet, controlled at 0.35 $\pm$ 0.01 cm^2. The volumetric evaporation rate (i.e. $\Delta V/\Delta t$) of this droplet-based evaporimeter was determined to be less than 2.7 µL/min, comparable to the basal tear production of healthy adults (i.e. 0.8–2.0 µL/min).[48,49]

Atomic Force Microscopy

Lateral structure and topography of the tear lipid films were studied with the combination of in situ Langmuir-Blodgett (LB) transfer from the CDS and atomic force microscopy
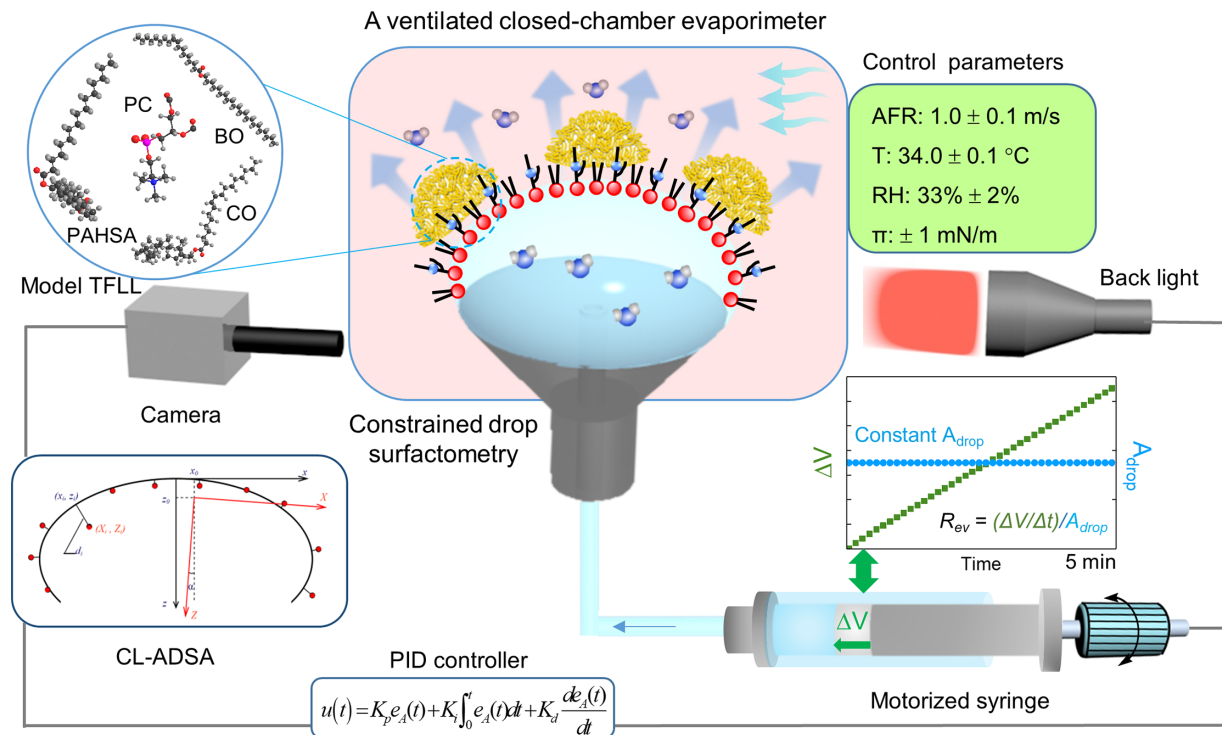
FIGURE 1. Schematic of a ventilated, closed-chamber, droplet evaporimeter with a constant surface area for studying evaporation resistance of the tear film lipid layer (TFLL). This droplet evaporimeter is constructed based on constrained drop surfactometry (CDS), in which a 5-mm water droplet (approximately 27 µL in volume and approximately 0.35 cm^2 in surface area) is constrained on a carefully machined pedestal with knife-sharp edges. The water droplet is enclosed in an environmental control chamber that ensures a rigorous control of experimental conditions, including the temperature, relative humidity (RH), and airflow rate (AFR). The surface area of the droplet is maintained at a constant using closed-loop axisymmetric drop shape analysis (CL-ADSA) with a proportional-integral-derivative (PID) control loop. The measuring principle of ADSA is illustrated in a box: ADSA determines the surface tension by numerically fitting the experimental droplet profiles (indicated by *red dots*) to theoretical droplet profiles (indicated by *black curves*) obtained with numerical integration of the Laplace equation of capillarity. The PID controller is illustrated by a PID control function with the proportional, integral, and derivative terms. The evaporation rate (R_{ev}, mm/min) is calculated as $(\Delta V/\Delta t)/A_{drop}$, where ΔV is the volume of water replenished into the droplet, in order to compensate for the water lost by evaporation. The Δt is the time period of the experiment, usually 5 minutes. The A_{drop} is the surface area of the droplet, controlled at 0.35 cm^2. The model TFLL consists of 40 mol% behenyl oleate (BO) and 40 mol% cholesteryl oleate (CO) that represent two nonpolar lipid classes (i.e. wax ester and cholesteryl ester in the natural TFLL), and 15 mol% phosphatidylcholine (PC) and 5 mol% palmitic-acid-9-hydroxy-stearic-acid (PAHSA) that represent two polar lipid classes in the natural TFLL (i.e. phospholipids and OAHFAs).

(AFM).[39,50] The lipid film was first LB transferred from the droplet by lifting a small piece of freshly peeled mica sheet at a speed of 1 mm/min. During the LB transfer process, the surface pressure of the lipid film was maintained at a constant ($\pm$ 1 mN/m). Topographical images of the lipid film were obtained with an Innova AFM (Bruker, Santa Barbara, CA, USA). Samples were scanned in air in contact mode and tapping mode. The contact mode used a silicon nitride cantilever with a spring constant of 0.12 N/m and a tip radius of 2 nm, whereas the tapping mode used a silicon cantilever with the spring constant of 42 N/m and a resonance frequency of 300 kHz. Relative height differences between domains were determined with section analysis using Nanoscope Analysis (version 1.5).

Statistical Analysis

All results were shown as mean $\pm$ standard deviation ($n = 10$ unless otherwise indicated). One-way ANOVA with Tukey's means comparison test was used to determine group differences (OriginPro, Northampton, MA, USA). A value $P < 0.05$ was considered to be statistically significant.

RESULTS AND DISCUSSION

Development of a Constant-Surface-Area Droplet Evaporimeter for Studying Evaporation Retardation by Lipid Films

Figure 2 demonstrates the capacity of this new evaporimeter in determining the rate of evaporation from a water droplet while maintaining a constant surface area of the droplet. Within a 5-minute period, the RH of the environment was maintained at 33%, whereas the temperature and airflow rate were controlled at 34°C and 1 m/s, respectively. Surface tension of the water droplet remained at a constant of 71 mN/m, indicating no contamination of the water surface. It can be seen that during the 5-minute period, in spite of water evaporation, the surface area and volume of the droplet were maintained at 0.35 cm^2 and 27 µL, respectively, using CL-ADSA (see Movie S1 of the Supplementary Data for this experiment). The volume of water replenished into the droplet, in order to maintain the constant surface area, increased linearly over the 5-minute period, with a volumetric rate of 2.7 µL/min. The water
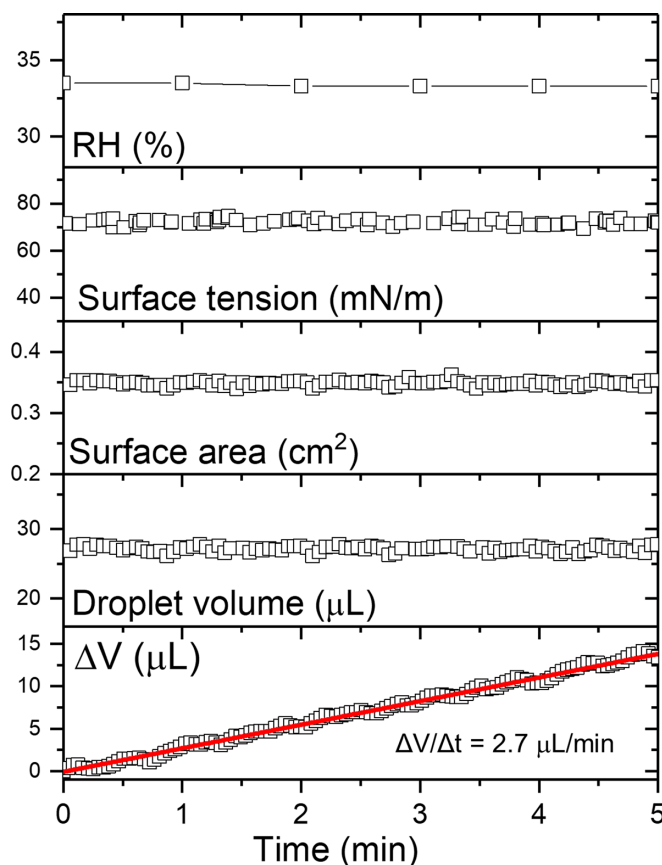
FIGURE 2. Typical experimental results for water evaporation determined within 5 min using the new droplet evaporimeter. Temperature and relative humidity (RH) were maintained at 34°C and 33%, respectively. Surface tension of water was relatively unchanged at 70 mN/m, indicating no contamination. Surface area of the droplet was actively controlled at a constant of 0.35 cm² using CL-ADSA. Volume of the droplet was relatively unchanged at 27 μL. The volumetric rate of water replenished into the droplet ($\Delta V/\Delta t$) to complement the water lost by evaporation was determined by linear regression (red solid line), corresponding to a volumetric evaporation rate of 2.7 μL/min.

evaporation rate ($\Delta V/\Delta t$)/A_{drop}, under the controlled experimental conditions, was determined to be 0.078 mm/min. As shown in Supplementary Figure S1 of the Supplementary Data, extending the experimental period to 15 minutes does not vary the water evaporation rate. Hence, the 5-minute experimental period is used thereafter.

To demonstrate the effect of lipid monolayers on water evaporation, we have studied the evaporation resistance of a DPPC monolayer at 34°C under various controlled surface pressures. DPPC (16:0, 16:0 PC) was selected as a model lipid monolayer because C16 fatty acids are able to balance the rigidity needed for a sufficient resistance to water evaporation and the "self-healing" effect after rupture by waves.[34]

As shown in Figure 3, effects of the DPPC monolayer on water evaporation can be roughly divided into three regions as a function of surface pressure. First, at 10 mN/m, the DPPC monolayer shows no statistically significant effect on water evaporation ($P > 0.05$ in comparison to the clean air-water surface). Second, at 20 and 30 mN/m, the DPPC monolayer shows moderate, but statistically significant ($P < 0.05$), effects on water evaporation, by reducing the evap-

oration rate by 4%. Third, at 40 and 50 mN/m, the DPPC monolayer shows significant retardation effects on water evaporation, with 9% and 17% reduction in the evaporation rate, respectively. These findings are in qualitative agreement with those reported by Miano et al. who determined the effect of the DPPC monolayer on water evaporation up to the surface pressure of 35 mN/m, at 36°C and 15% RH, using the pendant drop method.[40] These workers found that at the surface pressure below 12 mN/m, the DPPC monolayer showed no retardation effect on water evaporation. When the surface pressure was increased to 20 mN/m, the DPPC monolayer showed moderate effects on evaporation retardation, whereas increasing the surface pressure to 35 mN/m did not further increase the evaporation resistance.[40]

Figure 3 also shows the compression isotherm of the DPPC monolayer at 34°C, superimposed on the water evaporation data. The DPPC monolayer undergoes a liquid-expanded (LE) to tilted-condensed (TC) phase transition within the surface pressure range between 20 and 30 mN/m, indicated by a plateau region in the compression isotherm. (Reproducibility of this compression isotherm can be found in Supplementary Fig. S2.) This phase transition region of the DPPC monolayer at 34°C is in good agreement with our previous observations.[45] The LE-TC phase transition, or phase co-existence, can be visualized by the formation of TC domains approximately 1 nm higher than the surrounding LE phase, as demonstrated by the AFM image shown in the inset of Figure 3.

These findings suggest that the evaporation resistance of the DPPC monolayer is mainly determined by the phospholipid polymorphism. The LE-TC phase co-existence in the DPPC monolayer (i.e. at 20–30 mN/m), corresponds to region II in which the DPPC monolayer starts to show moderate resistance to water evaporation (see Fig. 3). At surface pressures lower than this phase transition pressure, the DPPC monolayer is in a disordered LE phase and hence does not significantly resist water evaporation (region I). At surface pressures higher than this phase transition pressure, the DPPC monolayer is compressed into a tightly packed, ordered TC phase, thus showing significant resistance to water evaporation (region III). These experimental data are in line with the theory of an active energy barrier to water evaporation through monolayers, originated from electrostatic and/or steric repulsions between lipid molecules upon monolayer compression.[35]

Effect of the Model TFLL on Water Evaporation

Figure 4a shows the quasi-static compression isotherms of three lipid films (i.e. egg PC, PAHSA, and a synthetic model TFLL), at 34°C. This model TFLL consists of 40 mol% BO and 40 mol% CO that represent two nonpolar lipid classes (i.e. wax ester and cholesteryl ester in the natural TFLL), and 15 mol% PC and 5 mol% PAHSA that represent two polar lipid classes in the natural TFLL (i.e. phospholipids and OAHFAs).[51] It should be noted that human meibomian lipids are composed of a complex mixture of more than 200 lipid species, primarily including cholesterol esters, wax esters, (O-acyl)-ω-hydroxy fatty acids, and triacylglycerols.[1,6] Modern lipidomics data further suggested that the polar lipid content in healthy TFLL is generally less than 5 mol%.[1,6] Hence, the model TFLL used here (i.e. BO:CO:PC:PAHSA [40:40:15:5]), is not only overly simplified in its lipid composition but also likely has an augmented abundance in polar lipids. Nevertheless, our previous studies have demonstrated that
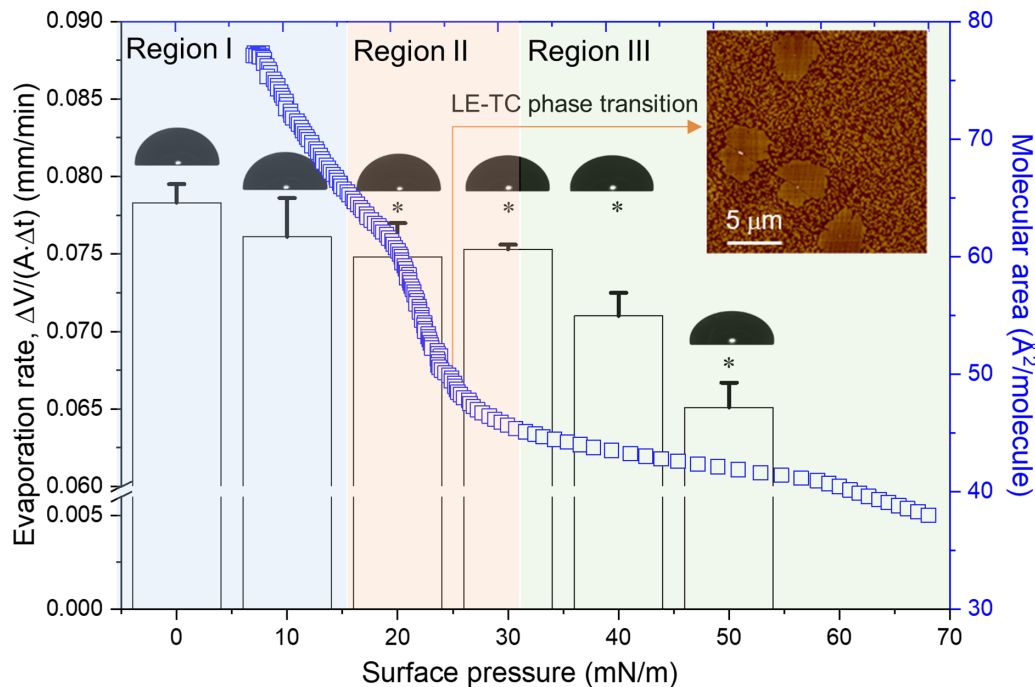
FIGURE 3. Superimposed compression isotherm of a DPPC monolayer at 34°C, and the corresponding evaporation resistance at various surface pressures. Surface pressure zero indicates a pure lipid-free air-water surface. The compression isotherm and evaporation resistance can be separated into three regions. Region I = No evaporation resistance for the DPPC monolayer in a disordered liquid-expanded (LE) phase; region II = Moderate evaporation resistance for the DPPC monolayer undergoing LE to tilted-condensed (TC) phase transitions; and region III = High evaporation resistance for the DPPC monolayer in a closely packed ordered TC phase. Insets are an AFM image showing LE-TC phase co-existence at 25 mN/m, and droplet images demonstrating the constant surface area. *$P < 0.05$ indicates statistically significant differences.

that this model TFLL represents the biophysical and rheological properties of the natural TFLL to a certain degree.[38,39]

Figures 4b to d shows the retardation effects of the PC, PAHSA, and model TFLL films at increasing surface pressures on water evaporation at 34°C. Because the PAHSA monolayer collapses at 34 mN/m, effects of the PAHSA monolayer on water evaporation were only studied for surface pressures up to 30 mN/m. It can be seen that all lipid films (i.e. PC, PAHSA, and the model TFLL), show statistically significant resistance to water evaporation, albeit to varying extents. For instance, at 30 mN/m, the PC, PAHSA, and model TFLL monolayers reduce the water evaporation rate by 2.5%, 4.8%, and 5.1%, respectively. For all studied lipid films, the retardation effect increases with increasing surface pressure. For example, the model TFLL reduces the water evaporation rate by 3.4% at 10 mN/m, 6.1% at 40 mN/m, and 11% at 47 mN/m (see Fig. 4d). Supplementary Figure S3 shows the curvature at the apex of the model TFLL-covered droplet upon increasing surface pressure. When the surface pressure increases from 0 to 47 mN/m, the curvature of the droplet decreases from 3.5 to 2.9 cm^{-1}. The curvature effect on droplet evaporation should be negligible for such moderately curved surfaces.

Our findings have a few novel implications in understanding the biophysical and physiological function of the TFLL. First, our study qualitatively addressed the discrepancy between available in vivo and in vitro studies about the effect of TFLL on water evaporation. Although in vivo studies in general predicted that the TFLL significantly reduced the rate of water evaporation from the corneal surface,[52,53] a vast majority of in vitro measurements were unable to

establish this finding.[26–32] Using various synthetic models, animal, or human meibomian lipids, numerous in vitro studies found no ($<1\%$)[26,28,30,31] or only limited (approximately 8% with an intense airflow of 2.5 m/s) evaporation resistance[29] in comparison to evaporation from the lipid-free air-water surface. Here, we found that a model TFLL was able to reduce the water evaporation rate up to 11% ($p < 0.001$; see Fig. 4d), thus indicating a definite evaporation resistance. This finding is attributed to the new ventilated, closed-chamber, constant-surface-area droplet evaporimeter developed in this study (see Fig. 1). This novel evaporimetry technique provides a rigorous environmental control, including temperature, relative humidity, airflow rate, surface area, and surface pressure, thus allowing for highly sensitive, reproducible measurements within a short period of only 5 minutes, whereas most gravimetrical methods require a least of 1-hour measurements.[28–30] It is worth mentioning that our method is essentially different from the sessile drop method used by Svitova and Lin.[41] To the best of our knowledge, the evaporimeter developed in this paper is the first and only in vitro evaporimetry technique capable of automatically controlling the constant surface area of a droplet without human intervention. This is done with the combination of CDS hardware and CL-ADSA software, both invented in our laboratory. In addition, no ventilation or airflow was introduced or controlled in those experiments by Svitova and Lin,[41] which may contribute to the low basal evaporation rate found in their experiments (i.e. approximately 0.16 µL/min), more than 15 times lower than the basal evaporation rate found in our experiments. Another factor that influences the evaporation rate is the temperature
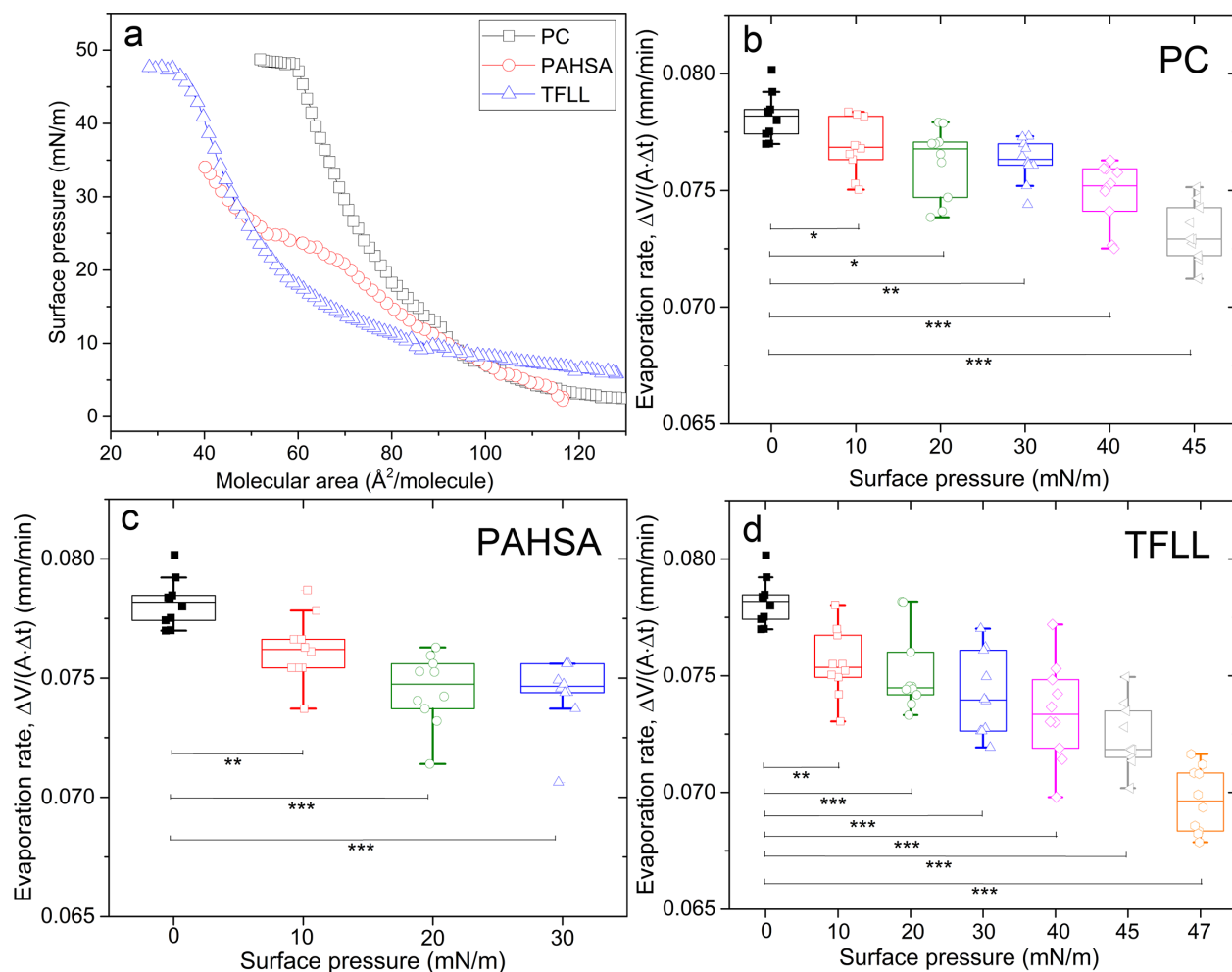
FIGURE 4. Effects of lipid films on water evaporation. (**a**) Compression isotherms of PC, PAHSA, and a model TFLL, BO:CO:PC:PAHSA (40:40:15:5). (**b-d**) Evaporation rates of water (mm/min) through PC, PAHSA, and the model TFLL at various surface pressures. *$P < 0.05$, **$P < 0.01$, ***$P < 0.001$.

differences between the environment and the surface of the evaporating droplet. Supplementary Figure S4 shows the surface temperature of the droplet under the controlled environmental temperature of 34°C. It can be seen that the airflow significantly affects the surface temperature of the droplet. Although without ventilation, there is only a 2°C temperature difference between the droplet surface and the environment, the temperature difference increases to 9°C with a 1 m/s airflow. Therefore, the in vitro evaporation rate determined here might be underestimated in comparison to in vivo conditions.

Second, our study showcases the importance of lipid packing density in evaporation resistance. As shown in Figure 4d, when the surface pressure is increased from 10 to 47 mN/m, the evaporation resistance of the TFLL increases by 3.2 times. Surface pressure 47 mN/m corresponds to a surface tension approximately 23 mN/m, which is significantly lower than the surface tension of whole tears but corresponds to the lowest surface tension of a highly compressed TFLL.[38]

Third, our study indicates that the long-chain nonpolar lipids may play a role in evaporation resistance of the TFLL. It has long been recognized that the evaporation resistance of polar lipid monolayers depends on both the chain length

and packing density of the lipid molecules.[33,34] La Mer and coworkers found that the evaporation resistance of saturated fatty acids was an exponential function of the chain length.[33,34] Any addition of one carbon atom in the hydrocarbon chain increases the evaporation resistance by a factor of 1.65.[15,33,34] However, the chain length effect of nonpolar lipids on water evaporation is largely unknown. Nonpolar lipids, such as wax esters and cholesteryl esters, account for 80% of the TFLL.[54] The model TFLL studied here contains 40% behenyl oleate (C22:0-C18:1) and 40% cholesteryl oleate (cholesterol-C18:1). Although these nonpolar lipids are incapable of directly spreading at the air-water surface, they somehow increase the evaporation resistance of the polar lipid monolayer (e.g. 4.2% for PC versus 6.1% for TFLL at 40 mN/m; see Figs. 4b vs. 4d).

Lateral Structure and Topography of the Model TFLL

Figure 5 shows the lateral structure and topography of three lipid films (i.e. PC, PAHSA, and the model TFLL made up of BO:CO:PC:PAHSA [40:40:15:5]), at 34°C. Reproducibility of these AFM images can be found in Supplementary Figures S5
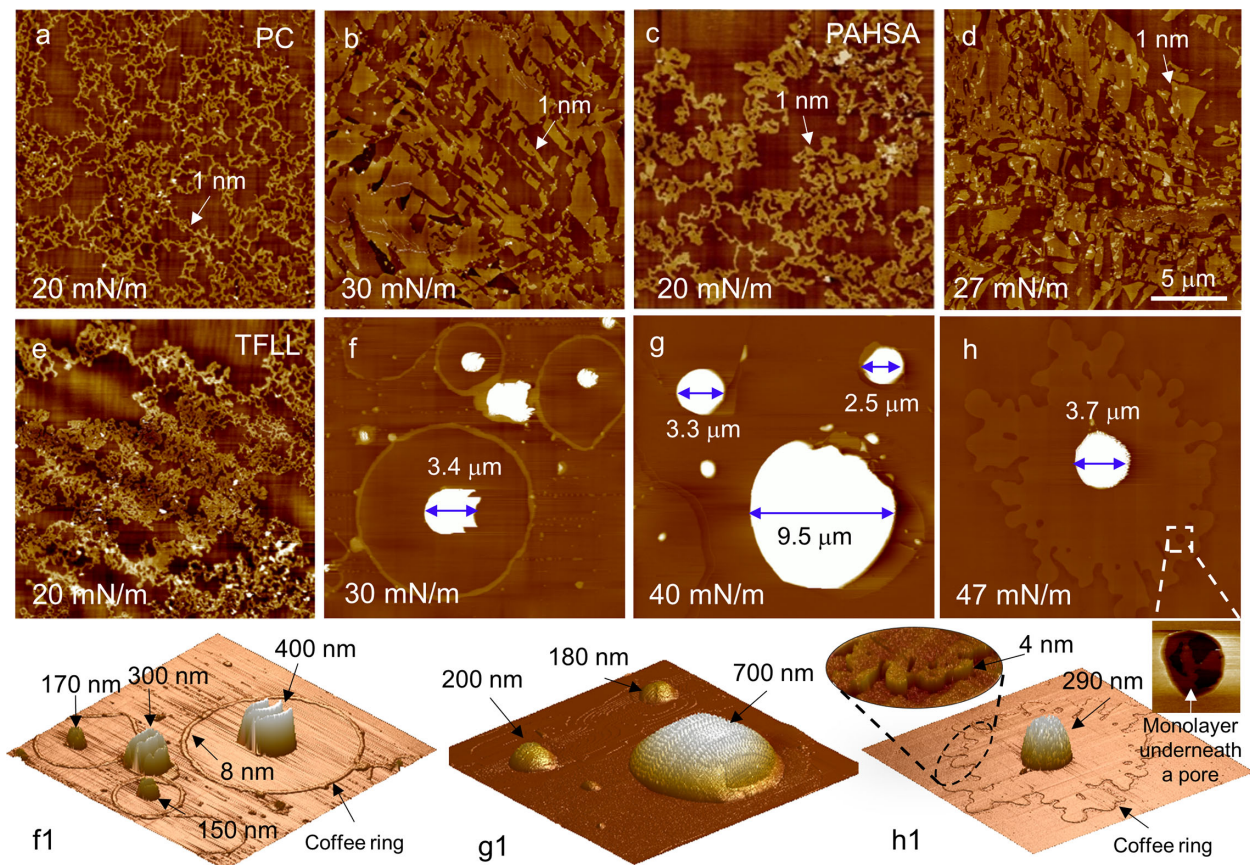
FIGURE 5. AFM topography and lateral structure of lipid films at various surface pressures. (**a, b**) PC monolayer at 20 and 30 mN/m. (**c, d**) PAHSA monolayer at 20 and 27 mN/m. (**e-h**) Model TFLL, BO:CO:PC:PAHSA (40:40:15:5) at 20, 30, 40, and 47 mN/m. (**f1-h1**) Three-dimensional renderings of the TFLL corresponding to AFM images shown in panels **f** to **h**. All AFM images have the same scanning area of 20×20 μm. The *z* range for images in **f** to **h** is 100 nm, whereas it is 5 nm for all other images. *Single-headed arrows* indicate the heights of the structures, whereas *double-headed arrows* indicate the lateral dimensions of the structures.

to S11. Films of the two polar lipids (i.e. PC; see Figs. 5a, 5b) and PAHSA (see Figs. 5c, 5d), assume a monolayer conformation with phase separation at surface pressures up to 30 mN/m. Lateral structures of the PC and PAHSA monolayers show a network of ramified, fiber-like ordered domains approximately 1 nm higher than the surrounding disordered phase. The network of the ordered domains increases in density upon increasing surface pressure from 20 to 30 mN/m, consistent with our previous observations.[39]

At a low surface pressure of 20 mN/m (see Fig. 5e), the model TFLL also demonstrates a general monolayer conformation with phase separation, similar to the polar lipids. However, at surface pressures equal to or higher than 30 mN/m (see Figs. 5f-h), the TFLL shows a completely different topography and lateral structure, compared to those of the polar lipid monolayers. At all high surface pressures (i.e. 30, 40, and 47 mN/m), the TFLL shows discrete bead-like structures ranging from approximately 150 to approximately 700 nm in height (see Figs. 5f1-h1 for three-dimensional renderings of the film topography). In comparison to lateral structures of the polar lipid films, the source of these high, bead-like structures must be the nonpolar lipids in the TFLL (i.e. BO and CO). Due to lack of affinity to water, these nonpolar lipids are squeezed out from the surface when the surface pressure is increased above 30 mN/m (corresponding to the surface tension of whole tears),

thus forming nonpolar lipid multilayers/aggregates residing atop the polar lipid monolayer.

Formation of nonpolar lipid droplets or aggregates by squeezing out from the TFLL at increasing surface pressure is supported by multiple experimental evidence. First, film compressibility of the TFLL significantly decreases at surface pressures higher than 30 mN/m (see Fig. 4a). Second, AFM has detected a unique evaporation pattern closely analogous to the coffee-ring effect.[55] These evaporation patterns have heights of either 4 nm (see inset of Fig. 5h1) or 8 nm (see Fig. 5f1), corresponding to 1 or 2 fully hydrated phospholipid bilayers. These "coffee-rings" are most likely formed by evaporation-driven self-assembly of reverse micelles of polar lipids mixed with the nonpolar lipids.[10,11] This also explains the various sizes of the oil "beads" found in the model TFLL, which could be a consequence of different degrees of oil evaporation and oil droplet coalescence. Third, AFM has revealed structures similar to the polar lipid monolayers (PC or PAHSA) underneath the nonpolar multilayer, as shown in a high-resolution (1×1 μm) AFM image scanned through a "pore" on the surface layer. This AFM observation provides direct evidence for layered structures of the TFLL.

Formation of the nonpolar lipid multilayer/aggregates in the TFLL corresponds to a slight increase in the evaporation resistance of the TFLL (see Figs. 4b, 4c vs. 4d). Therefore, the present study supports that the TFLL resists

water evaporation with a combined mechanism by increasing film compactness of the polar lipid film at the air-water surface, and, to a lesser extent, by increasing film thickness of the nonpolar lipid film. It should be noted that the model TFLL studied here only consists of four lipid components (i.e. BO:CO:PC:PAHSA [40:40:15:5]). Consequently, the squeezed-out nonpolar lipids formed discrete droplets/aggregates due to inadequate lipid mixing. Human meibomian lipids are composed of many different lipid classes, and each of these lipid classes consists of many homologous lipid species varying in lengths, degrees of unsaturation, and branching, which is essential for the natural meibomian lipids to have proper melting and lipid mixing.[1] Hence, the nonpolar lipid layer of natural TFLL is likely more continuous and more uniform than the model TFLL studied here, thus rendering more evaporation resistance.[56] However, more recent studies, both in vitro[57] and in vivo,[58,59] suggested that the thickness of the TFLL, and especially that of the nonpolar lipid layer of the TFLL, is not uniform but with regions of thicker lipid droplets or aggregates. Using in vitro surface rheological study of bovine meibomian lipids, Bhamla et al. also inferred that the TFLL is likely not uniform in thickness, with the thicker area acting as a more effective barrier to water evaporation.[60] These studies, including the present work, are consistent with the finding that tear film evaporation is not necessarily correlated with a uniform thickness of the TFLL.[61]

CONCLUSIONS

We have developed a novel ventilated, closed-chamber, droplet evaporimeter with a constant surface area for studying the effect of TFLL on water evaporation. This new evaporimeter is capable of a rigorous control of environmental conditions, including the temperature, relative humidity, airflow rate, surface area, and surface pressure, thus allowing for reproducible water evaporation measurements over a time period of only 5 minutes. The volumetric evaporation rate of this droplet evaporimeter is less than 2.7 µL/min, comparable to the basal tear production of healthy adults. With this new evaporimeter, we have established the in vitro evaporation resistance of a model TFLL that consists of 40% wax esters, 40% cholesteryl esters, and 20% polar lipids. It was found that the TFLL resists water evaporation with a combined mechanism by increasing film compactness of the polar lipid film at the air-water surface, and, to a lesser extent, by increasing film thickness of the nonpolar lipid film.

References

1. Butovich IA. Tear film lipids. *Exp Eye Res*. 2013;117:4–27.
2. Davidson HJ, Kuonen VJ. The tear film and ocular mucins. *Veterinary Ophthalmol*. 2004;7:71–77.
3. McCulley J, Shine W. A compositional based model for the tear film lipid layer. *Trans Am Ophthalmol Soc*. 1997;95:79.
4. King-Smith E, Fink B, Hill R, Koelling K, Tiffany J. The thickness of the tear film. *Curr Eye Res*. 2004;29:357–368.
5. Chen JZ, Green-Church KB, Nichols KK. Shotgun lipidomic analysis of human meibomian gland secretions with electrospray ionization tandem mass spectrometry. *Invest Ophthalmol Vis Sci*. 2010;51:6220–6231.
6. Brown SHJ, Kunnen CME, Duchoslav E, et al. A comparison of patient matched meibum and tear lipidomes. *Invest Ophthalmol Vis Sci*. 2013;54:7417–7423.
7. Butovich IA. The meibomian puzzle: Combining pieces together. *Prog Retinal Eye Res*. 2009;28:483–498.
8. Dean AW, Glasgow BJ. Mass Spectrometric Identification of Phospholipids in Human Tears and Tear Lipocalin. *Invest Ophthalmol Vis Sci*. 2012;53:1773–1782.
9. Paananen RO, Rantamäki AH, Holopainen JM. Antievaporative mechanism of wax esters: implications for the function of tear fluid. *Langmuir*. 2014;30:5897–5902.
10. Cwiklik L. Tear film lipid layer: A molecular level view. *Biochimica et Biophysica Acta (BBA) - Biomembranes*. 2016;1858:2421–2430.
11. Georgiev GA, Eftimov P, Yokoi N. Structure-function relationship of tear film lipid layer: A contemporary perspective. *Exp Eye Res*. 2017;163:17–28.
12. Butovich IA. Lipidomics of human Meibomian gland secretions: Chemistry, biophysics, and physiological role of Meibomian lipids. *Prog Lipid Res*. 2011;50:278–301.
13. Bron AJ, Tiffany JM, Gouveia SM, Yokoi N, Voon LW. Functional aspects of the tear film lipid layer. *Exp Eye Res*. 2004;78:347–360.
14. Millar TJ, Schuett BS. The real reason for having a meibomian lipid layer covering the outer surface of the tear film - A review. *Exp Eye Res*. 2015;137:125–138.
15. King-Smith PE, Bailey MD, Braun RJ. Four characteristics and a model of an effective tear film lipid layer (TFLL). *Ocul Surf*. 2013;11:236–245.
16. Willcox MDP, Argueso P, Georgiev GA, et al. TFOS DEWS II Tear Film Report. *Ocul Surf*. 2017;15:366–403.
17. King-Smith PE, Begley CG, Braun RJ. Mechanisms, imaging and structure of tear film breakup. *Ocul Surf*. 2018;16:4–30.
18. Nichols KK, Foulks GN, Bron AJ, et al. The International Workshop on Meibomian Gland Dysfunction: Executive Summary. *Invest Ophthalmol Vis Sci*. 2011;52:1922–1929.
19. Craig JP, Nichols KK, Akpek EK, et al. TFOS DEWS II Definition and Classification Report. *Ocul Surf*. 2017;15:276–283.
20. Stapleton F, Alves M, Bunya VY, et al. TFOS DEWS II Epidemiology Report. *Ocul Surf*. 2017;15:334–365.
21. Craig JP, Tomlinson A. Importance of the lipid layer in human tear film stability and evaporation. *Optometry Vis Sci*. 1997;74:8–13.
22. Mathers W. Evaporation from the ocular surface. *Exp Eye Res*. 2004;78:389–394.
23. Wong S, Murphy PJ, Jones L. Tear evaporation rates: What does the literature tell us? *Contact Lens Anterior Eye*. 2018;41:297–306.
24. Peng CC, Cerretani C, Li Y, et al. Flow Evaporimeter To Assess Evaporative Resistance of Human Tear-Film Lipid Layer. *Industrial Engineer Chem Res*. 2014;53:18130–18139.
25. Dursch TJ, Li W, Taraz B, Lin MC, Radke CJ. Tear-Film Evaporation Rate from Simultaneous Ocular-Surface Temperature and Tear-Breakup Area. *Optom Vis Sci*. 2018;95:5–12.
26. Rantamäki AH, Javanainen M, Vattulainen I, Holopainen JM. Do lipids retard the evaporation of the tear fluid? *Invest Ophthalmol Vis Sci*. 2012;53:6442–6447.
27. Borchman D, Foulks GN, Yappert MC, Mathews J, Leake K, Bell J. Factors affecting evaporation rates of tear film components measured in vitro. *Eye Contact Lens*. 2009;35:32–37.

28. Herok GH, Mudgil P, Millar TJ. The effect of Meibomian lipids and tear proteins on evaporation rate under controlled in vitro conditions. *Curr Eye Res*. 2009;34:589–597.

29. Cerretani CF, Ho NH, Radke CJ. Water-evaporation reduction by duplex films: application to the human tear film. *Adv Colloid Interface Sci*. 2013;197-198:33–57.

30. Sledge SM, Khimji H, Borchman D, et al. Evaporation and Hydrocarbon Chain Conformation of Surface Lipid Films. *Ocul Surf*. 2016;14:447–459.

31. Kulovesi P, Rantamäki AH, Holopainen JM. Surface Properties of Artificial Tear Film Lipid Layers: Effects of Wax Esters. *Invest Ophthalmol Vis Sci*. 2014;55:4448–4454.

32. Borchman D, Yappert MC, Milliner SE, et al. 13C and 1H NMR ester region resonance assignments and the composition of human infant and child meibum. *Exp Eye Res*. 2013;112:151–159.

33. Archer RJ, La Mer VK. The Rate of Evaporation of Water through Fatty Acid Monolayers. *Journal Physic Chem*. 1955;59:200–208.

34. Barnes GT, La Mer VK. The evaporation resistance of monolayers of long-chain acids and alcohols and their mixtures. In: La Mer VK (ed), *Retardation of Evaporation by Monolayers: Transport Processes*. New York, NY: Academic Press; 1962:9–33.

35. Blank M, La Mer VK. The energy barrier for monolayer penetration. In: La Mer VK (ed), *Retardation of Evaporation by Monolayers: Transport Processes*. New York, NY: Academic Press; 1962:59–66.

36. Tiffany JM, Winter N, Bliss G. Tear film stability and tear surface tension. *Curr Eye Res*. 1989;8:507–515.

37. Nagyová B, Tiffany JM. Components responsible for the surface tension of human tears. *Curr Eye Res*. 1999;19:4–11.

38. Xu X, Li G, Zuo YY. Biophysical properties of tear film lipid layer I. Surface tension and surface rheology. *Biophysical J*. 2022;121:439–450.

39. Xu X, Kang C, Sun R, Zuo YY. Biophysical properties of tear film lipid layer II. Polymorphism of FAHFA. *Biophysical J*. 2022;121:451–458.

40. Miano F, Calcara M, Giuliano F, Millar T, Enea V. Effect of meibomian lipid layer on evaporation of tears. *J Phys: Condensed Matter*. 2004;16:S2461.

41. Svitova TF, Lin MC. Evaporation retardation by model tear-lipid films: The roles of film aging, compositions and interfacial rheological properties. *Colloids and Surfaces B: Biointerfaces*. 2021;197:111392.

42. Mathers WD, Binarao G, Petroll M. Ocular water evaporation and the dry eye. A new measuring device. *Cornea*. 1993;12:335–340.

43. Rohit A, Ehrmann K, Naduvilath T, Willcox M, Stapleton F. Validating a new device for measuring tear evaporation rates. *Ophthalmic Physiol Opt*. 2014;34:53–62.

44. Valle RP, Wu T, Zuo YY. Biophysical influence of airborne carbon nanomaterials on natural pulmonary surfactant. *Acs Nano*. 2015;9:5413–5421.

45. Zuo YY, Chen R, Wang X, Yang J, Policova Z, Neumann AW. Phase transitions in Dipalmitoylphosphatidylcholine monolayers. *Langmuir*. 2016;32:8501–8506.

46. Yu K, Yang JL, Zuo YY. Automated droplet manipulation using Closed-Loop Axisymmetric Drop Shape Analysis. *Langmuir*. 2016;32:4820–4826.

47. Cândido C, de Dear R, Lamberts R. Combined thermal acceptability and air movement assessments in a hot humid climate. *Building and Environment*. 2011;46:379–385.

48. Mishima S, Gasset A, Klyce SD, Baum JL. Determination of Tear Volume and Tear Flow. *Invest Ophthalmol Vis Sci*. 1966;5:264–276.

49. Kim YH, Graham AD, Li W, Radke CJ, Lin MC. Human Lacrimal Production Rate and Wetted Length of Modified Schirmer's Tear Test Strips. *Transl Vis Sci Technol*. 2019; 8:40.

50. Xu L, Yang Y, Zuo YY. Atomic Force Microscopy Imaging of Adsorbed Pulmonary Surfactant Films. *Biophysical J*. 2020;119:756–766.

51. Butovich IA, Millar TJ, Ham BM. Understanding and analyzing meibomian lipids–a review. *Curr Eye Res*. 2008;33:405–420.

52. Mishima S, Maurice DM. The oily layer of the tear film and evaporation from the corneal surface. *Exp Eye Res*. 1961;1:39–45.

53. Goto E, Endo K, Suzuki A, Fujikura Y, Matsumoto Y, Tsubota K. Tear Evaporation Dynamics in Normal Subjects and Subjects with Obstructive Meibomian Gland Dysfunction. *Invest Ophthalmol Vis Sci*. 2003;44:533–539.

54. Chen J, Green KB, Nichols KK. Quantitative profiling of major neutral lipid classes in human meibum by direct infusion electrospray ionization mass spectrometry. *Invest Ophthalmol Vis Sci*. 2013;54:5730–5753.

55. Zhong X, Crivoi A, Duan F. Sessile nanofluid droplet drying. *Advances in Colloid Interface Sci*. 2015;217:13–30.

56. Rosenfeld L, Cerretani C, Leiske DL, Toney MF, Radke CJ, Fuller GG. Structural and rheological properties of meibomian lipid. *Invest Ophthalmol Vis Sci*. 2013;54:2720–2732.

57. Paananen RO, Viitaja T, Olżyńska A, Ekholm FS, Moilanen J, Cwiklik L. Interactions of polar lipids with cholesteryl ester multilayers elucidate tear film lipid layer structure. *Ocul Surf*. 2020;18:545–553.

58. Bai Y, Ngo W, Khanal S, Nichols JJ. Characterization of the thickness of the Tear Film Lipid Layer in Meibomian Gland Dysfunction using high resolution optical microscopy. *Ocul Surf*. 2022;24:34–39.

59. Bai Y, Ngo W, Nichols JJ. Characterization of the thickness of the tear film lipid layer using high resolution microscopy. *Ocul Surf*. 2019;17:356–359.

60. Bhamla MS, Chai C, Rabiah NI, Frostad JM, Fuller GG. Instability and Breakup of Model Tear Films. *Invest Ophthalmol Vis Sci*. 2016;57:949–958.

61. King-Smith PE, Reuter KS, Braun RJ, Nichols JJ, Nichols KK. Tear Film Breakup and Structure Studied by Simultaneous Video Recording of Fluorescence and Tear Film Lipid Layer Images. *Invest Ophthalmol Vis Sci*. 2013;54:4900–4909.

SUPPLEMENTARY MATERIAL

SUPPLEMENTARY MOVIE. Measurement of water evaporation from a water droplet for a time period of 5 minutes, while maintaining a constant surface area of the droplet at 0.35 cm^2.